Organic Geochemistry 195 (2024) 104842

Contents lists available at ScienceDirect

Organic Geochemistry

journal homepage: www.elsevier.com/locate/orggeochem

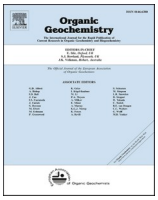

Fire-induced shifts in stalagmite organic matter mapped using Synchrotron infrared microspectroscopy

Liza K. McDonough [a,*], Micheline Campbell [c], Pauline C. Treble [a,c], Christopher Marjo [b], Silvia Frisia [c,d], Jitraporn Vongsvivut [e], Annaleise R. Klein [e], Viktoria Kovacs-Kis [f], Andy Baker [c]

[a] Australian Nuclear Science and Technology Organisation (ANSTO), New Illawarra Rd, Lucas Heights, NSW 2234, Australia
[b] Mark Wainwright Analytical Centre, UNSW Sydney, Sydney, NSW 2052, Australia
[c] School of Biological, Earth and Environmental Sciences, UNSW Sydney, NSW 2052, Australia
[d] School of Environmental and Life Sciences, University of Newcastle, NSW 2308, Australia
[e] ANSTO - Australian Synchrotron, Clayton, VIC 3168, Australia
[f] HUN-REN Centre for Energy Research, Konkoly-Thege Miklós u 29-33, H-1121 Budapest, Hungary

ARTICLE INFO

Associate Editor – Mark Fitzsimons

Keywords:
Speleothem
Paleoclimate
Fires
Synchrotron IRM
FTIR
HRTEM

ABSTRACT

Understanding organic matter (OM) in cave mineral deposits (speleothems) is essential for interpreting land use and climatic changes, and the incorporation of trace elements associated with organic compounds. However, the sources and composition of OM in speleothems are poorly understood due to challenges associated with measuring OM at low concentrations and the destructive nature of most speleothem OM analysis techniques. Synchrotron Fourier-transform infrared (FTIR) microspectroscopy is a promising non-destructive technique that can be used to investigate stalagmite OM composition. We use FTIR to analyse vegetation, soil, calcium carbonate and ash end-members and demonstrate the use of Synchrotron infrared microspectroscopy (IRM) mapping to detect temporal changes in the OM composition of a stalagmite from a shallow cave in south-west Western Australia. Our analysis reveals predominant FTIR peaks in the stalagmite linked to amides and CH_2 groups, suggesting potential microbial contributions, with smaller proportions of aromatic, CH_3 and C═O groups. High-resolution transmission electron microscopy revealed that this OM is likely hosted in sets of nanopores spaced hundreds of nanometers apart, aligned along calcite crystallographic orientations. Furthermore, we assess the impact of known wildfire events as discrete short term environmental changes on the stalagmite's OM composition. The temporal variability in OM functional group composition after fires implies complex fire-soil-vegetation-microbial interactions. This research demonstrates the effectiveness of Synchrotron IRM mapping in providing insights into the short and long-term environmental influences on stalagmite OM composition. Expanding this research to other regions and climates could further enhance the interpretation of OM changes in speleothem-based palaeoclimate reconstructions.

1. Introduction

Cave mineral formations (speleothems) are sensitive to surface environmental changes, including hydroclimate (Cheng et al., 2016) and vegetation cover (Baldini et al., 2005). These changes are commonly reflected in the geochemical composition (Blyth et al., 2008; Yang et al., 2011) and fabrics (Frisia et al., 2022) of speleothems over time. While most speleothem-based research has largely focused on the inorganic signals such as trace elements and stable isotopes ($\delta^{18}O$ and $\delta^{13}C$ of carbonate), major environmental events such as bushfires can also alter the organic matter (OM) content of speleothems (Argiriadis et al., 2019; Homann et al., 2022), indicating the importance of exploring novel techniques for understanding the use of OM as an environmental proxy.

Previous investigations of speleothem OM have been challenging, hampered by analytical difficulties associated with measuring the typically low concentrations (~0.01 to 0.3 %) of OM in cave deposits (Blyth et al., 2016). These low concentrations likely reflect low drip-water OM concentrations (Pearson et al., 2020) resulting from removal processes in the epikarst. Existing techniques for analysing OM in speleothems are often destructive and require large amounts of sample, resulting in low temporal resolution, or in the selective extraction of specific OM molecules (Li et al., 2014). However, recent methodological

* Corresponding author.
E-mail address: lizam@ansto.gov.au (L.K. McDonough).

https://doi.org/10.1016/j.orggeochem.2024.104842
Received 15 April 2024; Received in revised form 22 July 2024; Accepted 22 July 2024
Available online 25 July 2024

advancements have led to improved temporal resolution (e.g., Argiriadis et al. (2019)). Non-destructive spectrometric techniques, such as Synchrotron infrared microspectroscopy (IRM), in particular, enables spatial mapping of a sample at micrometre scales due to its small beam spot, thus offering high-resolution and high signal-to-noise ratio compared to traditional globar Fourier transform infrared (FTIR). Frisia and Borsato (2010) pioneered the use of Synchrotron IRM mapping to examine the OM content of a stalagmite from Grotta di Ernesto, an Alpine cave, revealing that the columnar calcite fabric incorporates OM interspersed within the calcite lattice, rather than within fluid inclusions. Other studies have employed benchtop offline FTIR to identify a soil source of humic and fulvic OM as the likely cause of an unusual red colouration in speleothems from Spain (Martínez-Pillado et al., 2020). More recently, the identification of aliphatic OM in speleothems has been linked to higher fluorescence using confocal microscopy, suggesting co-location of various OM compounds (Kost et al., 2023). FTIR, and in particular high-resolution mapping by Synchrotron IRM is therefore a potentially effective analytical tool in tracing changes in the OM composition of a sample, with the advantages of fast analyses, minimal preparation and being non-destructive.

FTIR analysis relies on the symmetric and asymmetric stretching and bending of functional groups within a molecule, referred to as vibrational modes. These modes exhibit characteristic absorption of infrared (IR) light at specific frequencies, which are influenced by factors such as atomic mass and the isotope of the element (i.e., the mass effect), as well as the types of atoms and bonds, and their molecular environment (i.e., the electronic effect). The composition of natural OM is highly complex, varying in the number and arrangement of atoms and bonds. For instance, humic and fulvic acids, which are commonly found in OM, possess conjugated pi-electron systems, aromatic rings, and double and triple bonds that can induce shifts in the location of C–H absorption bands on the IR spectrum. In contrast, OM such as microbial biomass and leaf material, which predominantly contains lipids and waxes with aliphatic C–H bonds, form carbon chains connected by single bonds (Mangold, 1969). The relatively simpler molecular structure of microbial biomass and leaf material make them less susceptible to the influence of surrounding atoms, bonds, and functional groups, resulting in more stable absorbance band positions.

Major environmental events such as bushfires can directly contribute to changes in speleothem OM, for example due to the production of polycyclic aromatic hydrocarbons (PAHs) (Perrette et al., 2008; Argiriadis et al., 2019; Argiriadis et al., 2024; Homann et al., 2022), levoglucosan, and lignin oxidation products (Homann et al., 2022). PAHs, which are characterised by aromatic rings, are produced by incomplete combustion of biomass and fossil fuels, with anthropogenic sources dominating in the modern period. Although an enrichment of PAHs has been observed in recent sediments compared to pre-industrial deposits (Wakeham et al., 1980; Perrette et al., 2008), in speleothems, potential 'memory effects' induced by storage of PAHs in the epikarst (Perrette et al., 2008), uncertainty around their transport in dripwater due to their hydrophobicity (Lamichhane et al., 2016), and high sorption make PAHs equivocal fire markers. Similarly, changes to other proposed molecular indicators of fire, such as hydrolysable sugars and lignin-derived phenolic monomers, showed no clear trend in soils after bushfires in Australia and their ability to act as reliable indicators of past fires is unclear (Mastrolonardo et al., 2015). Levoglucosan, a soluble, reactive anhydrosugar, is formed from the combustion of cellulose and hemicellulose at temperatures between 200 and 400 °C (Madsen et al., 2018), suggesting levoglucosan may be an indicator of low temperature burns. Levoglucosan has been used to identify past fire events in sediment cores (Elias et al., 2001) and snowpits (Kang et al., 2021), however the long-range transport of levoglucosan in fine particles means that it can be detected at a considerable distance from the source. Thus, the presence of levoglucosan may not necessarily be an indicator of a fire event occurring in the location that it is detected (Simoneit et al., 1999).

Indirect effects of fires on speleothem OM content may result due to fire-induced changes in soil chemistry and stoniness, and carbonate rock exfoliation (Shtober-Zisu and Wittenberg, 2021), which, most likely, would impact karst hydrology (Coleborn et al., 2018). For instance, the heating of calcium carbonate ($CaCO_3$) to form lime at high temperature increases both soil and drip water pH (Moropoulou et al., 2001; Hartland et al., 2010), which subsequently enhances the overall solubility of OM (Anderson et al., 2018). The solubilisation of soil OM and burnt biomass can enhance the transport of metals present in ash leachates by complexation with dissolved organic carbon (Chirenje et al., 2002; Hartland et al., 2012). These ash-derived metals have previously been identified as key indicators of fire events in the stalagmite record presented here (YD-S2) from south-west Western Australia (McDonough et al., 2022).

This study aims to identify functional group absorbance bands in FTIR analyses of stalagmite YD-S2, which contains a mineralogy of calcite, by using end-members including vegetation, precipitated and powdered $CaCO_3$, soils, and ash to understand the potential sources of OM in YD-S2. Previous research has identified variability in the size and shape of organic matter peaks under various soil and land cover types, vegetation types and burn temperatures (Solomon et al., 2005; Gao et al., 2022), thus we analyse ash, soils and vegetation collected from the region where the stalagmite grew to ensure the FTIR peaks reflect representative vegetation from the region. The identified peaks are then used as a baseline for the interpretation of the OM composition in stalagmite YD-S2 from southwest Western Australia (SW WA), previously studied by McDonough et al (2022). Transmission Electron Microscopy (TEM) is further used to provide an indication of how and where this OM may be incorporated into the stalagmite. By building on the findings of McDonough et al. (2022), who identified the timing of fire events in YD-S2 using ash-derived metals and phosphorus, the present research is the first preliminary investigation using Synchrotron IRM to investigate the impact of environmental changes on stalagmite OM composition.

1.1. Environmental setting and background

Stalagmite YD-S2 was collected from Yonderup Cave, a shallow cave, located in Yanchep National Park, SW WA. The cave roof is approximately 4 m below the ground surface, with little soil cover (<124 mm), and developed in the Tamala Limestone lithostratigraphic unit, which consists of Pleistocene aeolianite (Playford et al., 1976). The region is characterised by a Mediterranean climate, with most of its rainfall (56%) occurring in winter. YD-S2 contains dark, seasonal bands that occur throughout the stalagmite, which are interpreted to be the result of soil OM flushing at the onset of or during the wet season (McDonough et al., 2022). The geologic, climatic, and historical setting of the site is covered extensively in prior publications and is therefore only reported briefly here. The reader is directed to McDonough et al. (2022), Nagra et al. (2017) and Nagra et al. (2016) for further information on the sample location, site details and geologic context.

YD-S2 has a chronology spanning 245 years, from 1760 ± 13 to 2005 CE, over a length of 19 mm and an average annual growth rate of 76.7 μm ± 30.3 (1σ) (McDonough et al., 2022). The chronology was established by counting annual geochemical laminae (grey-scale image of thin section and Sr concentrations; McDonough et al., 2022) and has a maximum uncertainty of ±13 years. Previous studies have also examined the trace element composition of the stalagmite (Nagra et al., 2017), and investigated the impact of fire on its feeding dripwater trace element composition (Nagra et al., 2016).

McDonough et al. (2022) assessed changes in trace element composition in stalagmite YD-S2 during the timing of known fires which occurred in the Yonderup Cave's vicinity during the modern period (here referring to the 1960s onwards). These fires coincided with short-term peaks in speleothem phosphorus (P) and various metals such as zinc (Zn), copper (Cu), aluminium (Al) and lead (Pb), which principal component analysis (PCA) revealed loaded most strongly on PC3. These elements were interpreted to have been derived from ash, leading to the

conclusion that PC3 was an indicator of past fire events. The largest elemental peaks in the modern period were linked to a wildfire which occurred in 1977 CE and burned over 5 square kilometres of Yanchep National Park (Department of Environment and Conservation, 2010). Another large fire burnt in 1983 CE (Department of Environment and Conservation, 2010) which coincided with a small spike in Pb concentrations in YD-S2. A small fire was recorded near the cave in 1996 CE, followed by another small fire that burned directly over the cave in 2001 CE (Department of Biodiversity, 2020). These small fires were associated with spikes in Zn concentrations, and Al and Zn concentrations in the stalagmite, respectively (McDonough et al., 2022). Principal component analysis (PCA) was used to identify additional fire events that were not historically recorded, including those occurring in the pre-satellite and pre-European period. A particularly large previously unknown fire event was identified in 1897 ± 5 CE (9.35–9.45 mm DFT). This event led to elevated concentrations of P (up to 161 μg g^{-1}, 6.3 times higher than anywhere else in the record), and increased levels of Zn, Al, Cu and Pb in the stalagmite. This fire followed a multi-decadal dry period known as the Federation Drought (O'Donnell et al., 2021) which may have led to enhanced wildfire conditions. This also coincided with the arrival of European colonists, who may have used fire to clear vegetation or to locate cave entrances to develop these as tourist attractions (Campbell et al., 2023). This shift in land use appears to have resulted in a shift from more frequent lower intensity fires to less frequent higher intensity fires (McDonough et al., 2022). Other likely fire events were also identified, including a previously (unrecorded) fire in 1990 CE inferred by peaks in P, Zn and Al.

2. Methods

2.1. FTIR analysis of reference materials

Reference materials (used as calibration end-members) were analysed using an offline Hyperion 3000 microscope connected to a Bruker VERTEX v70 spectrometer using a traditional globar source IR at the Australian Synchrotron. These reference materials included precipitated $CaCO_3$ powder, humic acid (HA), natural organic matter (NOM) and fulvic acid (FA) powder standards from the International Humic Substances Society (IHSS, standard numbers 2S101H, 1R101N and 1S101F). We also took the opportunity to analyse powdered leaves, stems and seeds from vegetation in SW WA, ash from fires in SW WA and southeast Australia, and soils from the SW WA region. These materials had been collected opportunistically over the last seven years and stored at ambient temperatures in the laboratory and have therefore likely undergone some degree of degradation. These materials were used to compare against the spectra obtained from YD-S2. The vegetation powders were collected from above Golgotha Cave in the Boranup Forest in 2017 and include typical SW WA vegetation stems, seeds, and leaves, including those from *Agonis flexuosa*, *Bossiaea disticha*, *Corymbia calophylla*, *Hakea*, *Macrozamia riedlei*, *Templetonia retusan*, *Xanthorrhoea preissii* and Eucalyptus species (Fig. S1). Vegetation and soil samples were collected in plastic bags, dried at 60 °C for 48 h, ground using a ball grinder and stored in polypropylene centrifuge tubes at ambient temperatures. Soil samples were collected from above caves in SW WA in the Margaret River region including Golgotha Cave, Jewel Cave, Crystal Cave and Moondyne Cave, and in Yanchep, including Yonderup Cave and Minnies Grotto. Ash samples ranging in colour from black to white were collected after a bushfire in Macleay (New South Wales, Australia) in 2020 and after fires occurring in the SW WA region including Calgardup (2018), Yanchep (2020) and Golgotha (2022). Ash and soil samples were stored dry in low density polyethylene bags at ambient temperatures.

2.2. Synchrotron-radiation based high-resolution infrared spectroscopy

The YD-S2 thick section was cut from the central growth axis of the stalagmite using a water-cooled diamond saw, embedded in Epofix (Struers) epoxy, and polished to 1 μm using a diamond polishing paste (see Nagra et al., 2016). Contamination with exogenous OM is an important consideration in speleothem OM studies (Wynn and Brocks, 2014). We therefore took steps to minimise any potential contamination by sonicating the sample in ultrapure water after polishing and drying the sample at ambient temperatures. Immediately prior to IRM analysis, the sample surface was cleaned with analytical reagent grade ethanol (pure 100 % ethanol with no water content). Preliminary testing of the epoxy surrounding the outside of the sample was also undertaken. Fig. S2 shows that there are differences in the peak heights and ratios between the stalagmite and the epoxy. For example, an aromatic peak at ~1510 cm^{-1} is much higher than the amide II peak in the resin, whilst in the stalagmite the aromatic peak is much lower than the amide II peak. Additionally, the aromatic 1610 cm^{-1} peak is much higher compared to the amide I peak next to it in the epoxy, whilst in the stalagmite, the aromatic peak at 1610 cm^{-1} is not clearly observed. These differences in peak presence and heights, as well as our use of a thick section (~2 mm thick), suggest the OM is not sourced from epoxy contamination.

IRM maps were collected over regions of YD-S2 using an online Bruker VERTEX 80v FTIR spectrometer equipped with a Hyperion 3000 infrared microscope at the Australian Synchrotron's IRM beamline during two experiments. Analyses utilised attenuated total reflectance (ATR) FTIR microspectroscopy with a germanium (Ge) crystal, a scanner velocity of 40 kHz, an aperture setting of 0.5 mm, a pinhole of 4.4 μm and a 20x ATR objective. Preliminary tests of the sample were undertaken to determine ideal contact pressure prior to mapping, with greater pressure between the Ge crystal and YD-S2 required to enhance the weaker OM peaks in the sample (Fig. S3).

Three relatively low-resolution maps were collected over YD-S2 in March 2022 (Experiment 1), including one map over the inferred large fire event in 1897 CE (McDonough et al., 2022), and two maps covering historically recorded fires in 1977 CE, 1983 CE, 1996 CE and 2001 CE (Department of Biodiversity, 2020) and the additional fire inferred by McDonough et al. (2022) in 1990 CE (Table 1). It is noted that the fire event in 1996 CE was relatively small and did not pass over the top of the cave, however the fire burned within < 10 m from the cave and a peak in ash-derived metals appears in the YD-S2 record, indicating likely ash deposition above the cave (McDonough et al., 2022). Table 1 details the experimental setup for the IRM analyses. In total, six fire events were analysed. All six were analysed at relatively low resolution, and the 1897 CE and 1977 CE events were additionally analysed at high-resolution. Low-resolution maps (Map 2, Map 6, and Map 7) had x and y step-sizes of 10–50 μm, while high-resolution maps (Map 4 and Map 5) had x and y step-sizes of 5 μm (Table 1).

2.3. Transmission Electron Microscopy

A lamella was cut from a polished thin section and a region approximately 5 × 5 μm wide and 2 μm deep was thinned using a Thermo Scientific Scios 2 Dual Beam focused ion beam scanning electron microscope (FIB-SEM) instrument. The Focused Ion Beam (FIB) lamella was cut parallel to the vertical growth axis of the stalagmite. The thin section needed to be preserved as it was, thus carbon coating was avoided and the positioning of the area to be cut was guided by etching a mark on the glass portion of the thin section adjacent to the 1897 CE fire layer. Subsequent inspection at high magnification under the optical microscope revealed that the FIB lamella was taken near the top of the 1897 CE fire layer.

The lamella extracted from the thin section was then thinned *in-situ* in the FIB-SEM to obtain electron transparency with low-energy ions to minimize surface damage to the sample. The electron transparent region was then observed with a Thermo Fisher Scientific THEMIS 200 G3 microscope with a spherical aberration-corrected objective lens (FEG electron source, point resolution 0.07 nm in HRTEM mode) equipped with FEI Super-X EDS detection system. During measurements the TEM

Table 1
Parameters used for lower resolution (lower res.) and higher resolution (higher res.) micro-ATR mapping over fire events in stalagmite YD-S2 from Yonderup Cave, Western Australia during two Synchrotron IRM experiments. DFT refers to distance from the youngest end (top) of the stalagmite.

Map ID	Map 2 (1897 fire)	Map 6 (1977 fire)	Map 7 (2001, 1996 and 1990 fires)	Map 4 (1897 fire)	Map 5 (1977 fire)
Experiment #	1	1	1	2	2
Map type	Lower res.	Lower res.	Lower res.	Higher res.	Higher res.
Mapped region	6.40–10.40 mm DFT	1.37–2.67 mm DFT	0.13–1.43 mm DFT	9.05–9.60 mm DFT	1.95–2.50 mm DFT
Map run time (hours)	6.7	13.0	13.0	7.3	7.3
Aperture setting	0.5 mm				
Pinhole	4.4 μm				
Objective	20x				
Scanner velocity	40 kHz				
X distance	500 μm	600 μm	600 μm	100 μm	100 μm
Y distance	4000 μm	1300 μm	1300 μm	550 μm	550 μm
X step	50 μm	20 μm	20 μm	5 μm	5 μm
Y step	20 μm	10 μm	10 μm	5 μm	5 μm
# of points collected along X	10	30	30	20	20
# of points collected along Y	200	130	130	110	110
# of scans per point	16				

was operating at 200 kV accelerating voltage. Bright-field TEM (BFTEM), high-resolution TEM (HRTEM) and selected area electron diffraction (SAED) patterns were obtained. SAED patterns were taken inserting a 200-μm-sized aperture, which provides a diffraction area of approximately 3 μm diameter. The SAED patterns were taken by tilting the specimen holder stage so that the beam was parallel to a zone axis and the diffraction pattern recorded major calcite orientations. High angle annular dark field imaging (HAADF) was used for the assessment of the average density before mapping elemental distribution in Scanning Transmission Electron Microscopy (STEM) mode. For trace elements, counts had very low statistics. To reduce beam damage, the microscope setting was aimed at producing a low beam current. The HRTEM image, as well as EDS spectrum images, were recorded by a 4 k × 4 k Ceta camera using Velox software (Thermo Fisher).

2.4. FTIR data post-processing

YD-S2 Synchrotron IRM maps were water-vapour and aqueous-corrected in Bruker OPUS (https://www.bruker.com), then imported into CytoSpec (www.cytospec.com), cropped to wavenumbers 1150–3500 cm^{-1} (to remove noisy ends of the spectra) and then noise-reduced. Inverted second derivatives of the offline reference spectra as well as the water-corrected, cropped and noise reduced YD-S2 spectral maps were calculated using a second order Savitzky-Golay filter with 21 smoothing points (Savitzky and Golay, 1964). Here we used the second derivative for peak identification. The second derivative can reduce baseline impacts and compensate for instrumental drift and has the advantage of enhancing small spectral peaks. Care should be taken with interpretation, as it can increase noise in the signal, although this can be overcome by the smoothing used. Maps were assessed individually to prevent any impact of variation in contact pressure between the two experiments on the interpretation.

Maps of the second derivative absorbance intensity of individual peaks (summed absorbance intensity of each peak from trough to trough) were converted to greyscale. Maps were then exported and loaded into ImageJ software (Schneider et al., 2012), where line profiles of greyscale values were extracted using a 100-pixel line width. Greyscale values represent relative concentrations with higher values indicating higher summed absorbance intensity and lower values indicating lower summed absorbance intensity. Breusch-Pagan tests and Shapiro-Wilk tests were undertaken and confirmed that the data are heteroscedastic and non-normal ($p < 0.001$ for both tests, for all variables). Robust regression models were undertaken using the 'rlm' function in the Statsmodels package in Python (Seabold and Perktold, 2010) as this method does not require assumptions of homoscedasticity and normality to be met as they give less weight to observations with large residuals, preventing the larger scale residuals from dominating the estimation process. Each model used a different IR peak as a response variable and all other IR peaks as predictor variables to examine the relationships between the peaks. The analysis also included second order polynomial terms for each predictor and interaction terms between all pairs of predictors. The second order polynomial helps to capture non-linear relationships of each predictor with the response variable whilst the interaction terms help to capture the effect of two variables acting together on the response variable. The coefficients reflect changes in the response variable when there is a one-unit change in the predictor variable whilst holding all other variables and interaction terms in the model constant.

FTIR peaks associated with the CH_3/CH_2 ratio were used to understand changes in the ratios of OM containing methyl (CH_3) or methylene (CH_2) groups (Lin and Patrick Ritz, 1993). An increase in the CH_3/CH_2 ratio is indicative of an increase in branching and/or removal of the methylene group and/or decline in chain length of the hydrocarbon moiety (Igisu et al., 2018a). In contrast, low CH_3/CH_2 ratios are indicative of long, straight hydrocarbon moieties, including bacterial membrane lipids (Igisu et al., 2009). CH_3/CH_2 ratios were calculated according to the $\nu_{as}(CH_3)$ and $\nu_{as}(CH_2)$ band locations (ratio of the second derivative absorbance intensity at 2950–2975 cm^{-1}/2906–2949 cm^{-1}).

3. Results and discussion

3.1. Identification of aromatic, aliphatic and carbonate absorbance bands

In the 2800–3050 cm^{-1} (C–H stretching) region, the bulk vegetation reference powders exhibited three distinct asymmetric and symmetric C–H vibrational absorbance bands, denoted as $\nu_{as}(CH_3)$, $\nu_{as}(CH_2)$, and $\nu_s(CH_2)$ bands. These bands were identified at approximately 2963 cm^{-1}, 2920 cm^{-1}, and 2851 cm^{-1}, respectively (indicated by black vertical dashed lines in Fig. 1A, 1B, and 1D). Notably, the most prominent peaks are observed in the $\nu(CH_2)$ bands. IHSS OM standards show higher ν(CH) absorbance band frequencies (wavenumbers) compared to the vegetation standards, with the peaks in the spectra of IHSS standards shifted to higher wavenumbers on the x-axis in the C–H stretching region, as indicated by the green dashed lines (Fig. 1B).

We also examined peaks in the fingerprint region of the spectrum, which refers to the spectral features at lower wavenumbers (1420–1780 cm^{-1}). The fingerprint region differs from the C–H stretching region at higher wavenumbers as it encompasses a wide range of vibrational modes from various parts of the molecule. The pattern of peaks in the fingerprint region are unique to each compound, providing a "fingerprint" that allows for the overall identification of different substances. The fingerprint region of the vegetation standards spectra shows a C═O absorbance band aligning with C═O in carboxylic acids (COOH;

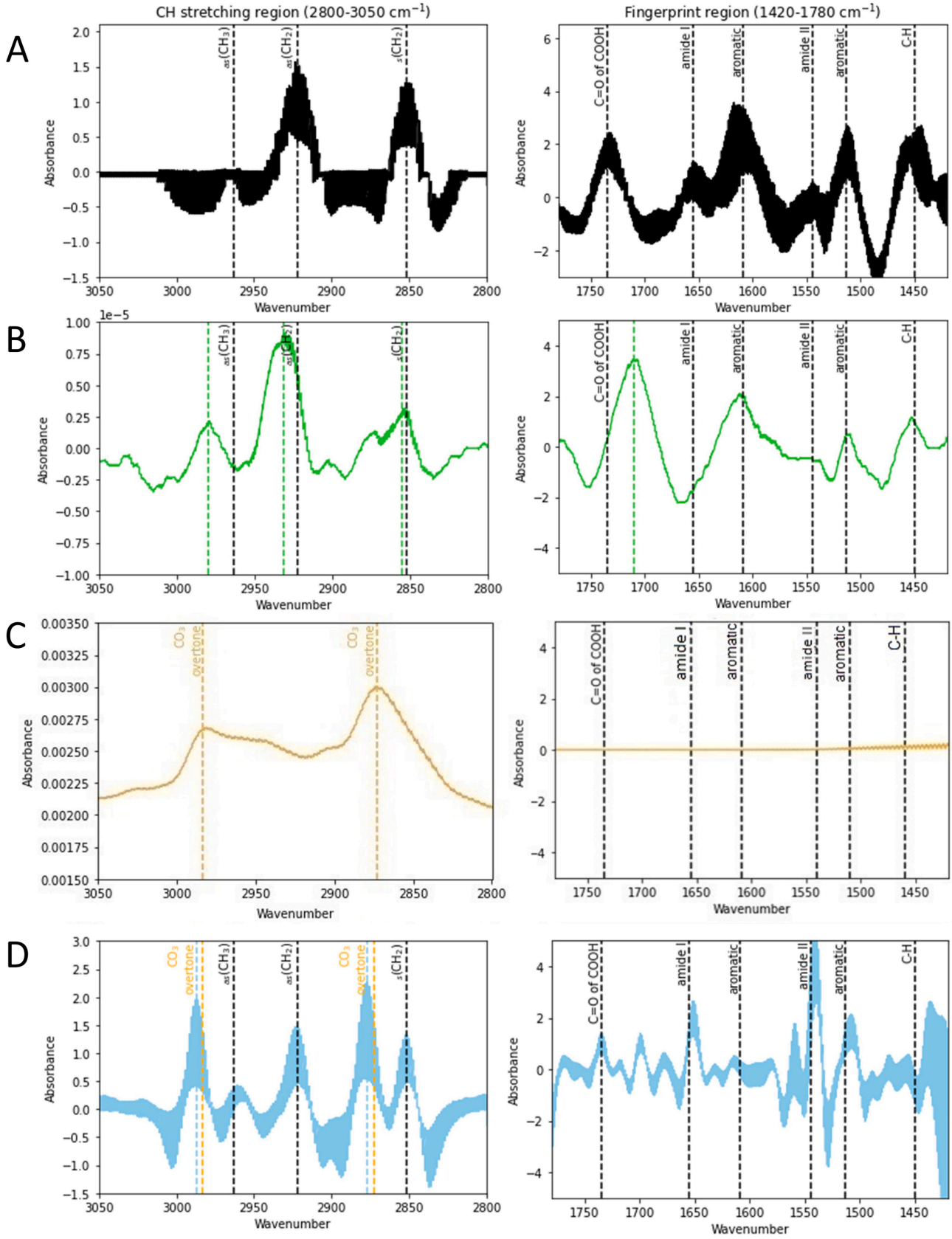

(caption on next page)

Fig. 1. Spectra from A) vegetation powders (n = 29, see also Fig. S1), B) International Humic Substances Society (IHSS) standards (n = 3), C) precipitated and powdered $CaCO_3$ (n = 1), and D) YD-S2 stalagmite (n = 25). Shaded regions represent the upper and lower absorbance values. C–H stretching regions (2800–3050 cm^{-1}) of the spectra are shown to the left whilst the fingerprint regions (1420–1780 cm^{-1}) are shown to the right. Note: Pure vegetation powder (A; black spectrum) shows three key aliphatic ν(CH) absorbance bands (vertical black dashed lines) in the 2800–3050 cm^{-1} region. These are identified at ~ 2963 cm^{-1} ($\nu_{as}(CH_3)$), ~2920 cm^{-1} ($\nu_{as}(CH_2)$), and ~ 2851 cm^{-1} ($\nu_{s}(CH_2)$). Six key carboxylic acid, aromatic and aliphatic peaks are identified in the 1420–1780 cm^{-1} region in the vegetation and IHSS spectra. The YD-S2 stalagmite crystal (D; blue spectrum) reveals a combination of the three main C–H bands, the two carbonate absorbance bands and the organic absorbance bands located in the fingerprint region in various ratios (note that C═O of COOH peak is located at a lower frequency in the IHSS standards compared to the vegetation powder). The C–H stretching region displayed in C represents the original spectrum for visual peak clarity whilst all other spectra represent the inverted second derivative values that have been centred to the mean, scaled to the standard deviation, and smoothed using a Savitzky-Golay filter using a window size of 21. (For interpretation of the references to colour in this figure legend, the reader is referred to the web version of this article.)

Benning et al. (2004); Nuzzo et al. (2020)) observed at 1735 cm^{-1} (N.B. this peak is located at a lower wavenumber in the IHSS FA, HA and NOM standards), and an aromatic absorbance band observed at 1608 cm^{-1}, typically ascribed to C═C, H-bonded C═O of conjugated ketones and symmetric stretching of COO– groups, respectively (Olk et al., 2000; He et al., 2009; Soong et al., 2015). A C–H absorbance band is also located at 1446 cm^{-1} (Arocena et al., 1995; Stevenson, 1994). Other absorbance bands corresponding to aromatic, amide II (CNH) and amide I (C═O) peaks are present at 1513 cm^{-1}, 1545 cm^{-1} and 1653 cm^{-1}, respectively (Montecchio et al., 2006; Jardine et al., 2017; Igisu et al., 2018b). Notably, the amide I peak is not visible in the spectra of IHSS standards (Fig. 1B) (Table 2).

In the powdered precipitated $CaCO_3$ (Fig. 1C), CO_3^{2-} (carbonate) overtones are identified at ~ 2876 cm^{-1} and ~2981 cm^{-1} (Galván-Ruiz et al., 2009; Arrizabalaga et al., 2015; Stanienda-Pilecki, 2019; Pejcic et al., 2021) which may interfere with the observation of C–H stretching bands in the aliphatic (2800–3050 cm^{-1}) region of stalagmites. The YD-S2 stalagmite spectra (Fig. 1D) reveal a combination of three main C–H stretching bands identified in vegetation standards and two carbonate absorbance bands identified in the $CaCO_3$ standards. Notably, an offset in the CO_3^{2-} peak height and positioning is observed between the powdered reference material (orange dashed line) and the YD-S2 crystalline sample (blue dashed lines) in Fig. 1D (see also Fig. S4), likely due to homogenisation of the material when powdered.

In the 1420–1780 cm^{-1} fingerprint region, YD-S2 spectra display absorbance bands primarily aligning with amide I and amide II peaks at 1651 cm^{-1} and 1540 cm^{-1}, respectively. These absorbance bands represent peptides and proteins and can be characteristic of microbial biomass (Benning et al., 2004; Montecchio et al., 2006). The C═O absorbance band representing the carboxylic acid functional group, is also observed at 1735 cm^{-1}. This peak is also observed in the vegetation "end member" spectra (Fig. 1A) and has also been observed in FTIR spectra of microbial biofilm matrix comprised of exopolysaccharides, extracellular proteins, lipids and nucleic acids (Kamnev et al., 2023; Naumann et al., 1988).

Table 2
IR peaks identified, and peak locations (wavenumber, cm^{-1}) for vegetation powders, stalagmite YD-S2 and IHSS organic matter humic acid (HA), natural organic matter (NOM) and fulvic acid (FA) standards used in the current study.

Stretching vibration	Vegetation powder IR peak location (cm^{-1})	Stalagmite IR peak location (cm^{-1})	IHSS standards IR peak location (cm^{-1})	Calcite IR peak location (cm^{-1})
CO_3 overtone	NA	~2987	NA	~2981
CH_3 (as)	~2963	~2959	~2980 (FA/NOM) ~1977 (HA)	NA
CH_2 (as)	~2920	~2922	~2927 (HA/NOM) ~2938 (FA)	NA
CO_3 overtone	NA	~2878	NA	~2876
CH_2 (s)	~2851	~2851	~2862	NA
C═O of COOH	~1735	~1735	~1710	NA
Amide I	~1653	~1651	N/A	NA
Aromatic	~1608	~1613	~1611	NA
Amide II	~1545	~1540	~1547	NA
Aromatic	~1513	~1509	~1512	NA
CH_2 def	~1446	NA	~1452	NA

3.2. Comparison of organic matter spectra in vegetation, soil, and ash

Vegetation contains organic peaks with greater absorbance, suggesting more organic abundance compared to soils and ashes (Fig. 2). Vegetation contains high peak absorbance values of the aromatic peak at 1610 cm^{-1} and carboxyl groups (═O of COOH) which are not present in soils (Fig. 2B) and ash (Fig. 2C and Fig. 2D), indicating removal of these compounds when plants are combusted. Other organic peaks present in the vegetation are detectable in the soil, but at reduced peak absorbance intensities. Notably, aromatics appear to be retained in the soils (Fig. 2B), which is expected due to adsorption of aromatic OM molecules to mineral surfaces, including calcite (Nikolenko, 2001). In black ash, removal of most OM groups aside from aromatic and amide I groups (Fig. 2C) suggests persistence or formation of aromatic compounds (e.g., PAHs) in incompletely combusted plant material (Fisher et al., 2002; Masto et al., 2015), and possible presence of amides due to microbial activity (Kleber, 2022). White ash spectra are dominated by a CO_3^{2-} peak and negligible organic peaks apart from very small amide I and C–H peaks (Fig. 2D). The near complete lack of organic peaks in white ash reflects the more complete combustion of OM at high temperatures, and the formation of $CaCO_3$ at temperatures between ~ 500 and ~ 700 °C (Mastrolonardo et al., 2014).

3.3. The organic matter IR signal of stalagmite YD-S2

For stalagmite YD-S2, the amide II band (CNH) shows the highest intensity peak in the fingerprint region, followed by amide I and an aromatic peak located between 1495 and 1530 cm^{-1}, whilst CH_2 peaks are dominant in the C–H stretching region, aside from the CO_3^{2-} overtones (Fig. 1D). Regression models were undertaken using the data from the three largest YD-S2 maps to identify which organic matter peaks were the best predictors for these functional groups in the stalagmite. The results summarised in Fig. 3 suggest that: I) amide II is best predicted by C═O of COOH and aromatic peaks (coefficients of 1.09 and 2.44, both $p < 0.001$), II) amide I is best predicted by positive $\nu_{as}(CH_2)$ and negative $\nu_{as}(CH_3)$ (coefficients of 1.37 and −0.69, both $p < 0.001$), III) the aromatic peak at 1495–1530 cm^{-1} is best predicted by C═O of COOH and amide I (0.38 and 0.52 respectively, $p = 0.022$ and $p = 0.002$ respectively), and IV) $\nu_{as}(CH_2)$ is best predicted by C═O of COOH and aromatic groups (0.41 and 0.42 respectively, both $p < 0.001$). These coefficients indicate that, despite both the amide peaks being associated with proteins, there might be a different source (or process) underpinning the presence of each peak in YD-S2, with amide I (C═O) associated with long-chain aliphatics, and amide II (C-N–H) associated with aromatics, potentially as aromatic amino acids.

3.3.1. Impact of fire on the organic matter Synchrotron IRM signal of stalagmite YD-S2

TEM was undertaken on the layer corresponding to the 1897 CE fire event (McDonough et al., 2022) in order to understand how the OM

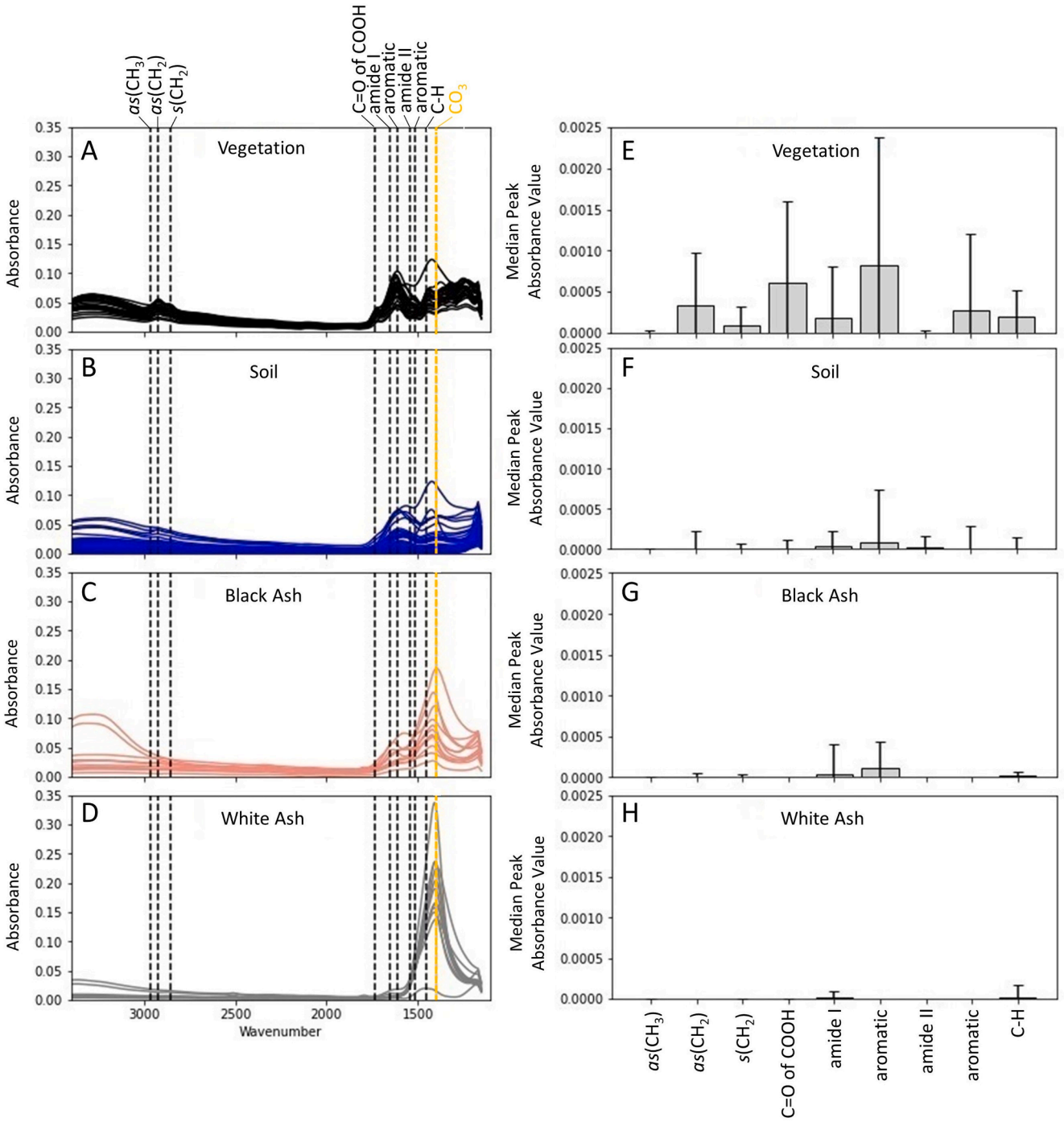

Fig. 2. Original spectra (left) with bar plots (right) showing the median inverted second derivative peak absorbance values (whiskers represent the maximum value) from A) vegetation powders, B) soil, C) black ash, and D) white ash. Black vertical dashed lines in the original spectra represent the organic peaks identified in Fig. 1. The orange vertical dashed line represents the main (v3) CO_3^{2-} absorbance band at approximately 1405 cm^{-1}. Bar plots display organic matter absorbance bands on the x-axis for E) vegetation powders, F) soil, G) black ash, and D) white ash. See Fig. S5 for representative spectra from each sample type plotted individually. (For interpretation of the references to colour in this figure legend, the reader is referred to the web version of this article.)

observed in the IRM data presented above is incorporated into the stalagmite. Post-fire speleothem OM composition is likely to be influenced by the re-establishment of vegetation communities and microbial activity, which is in part controlled by fire frequency, fire severity, soil conditions, and the soil seed bank (Kozlowski, 2002). Severe fires may trigger changes in soil hydrophobicity due to high burning temperatures (González-Pérez et al., 2004; Moya et al., 2019; Yan et al., 2020), and reduce microbial OM (Coleborn et al., 2016), whilst a lower intensity burn may result in the deposition of partially burnt plant material to soils, increasing soil OM availability (Ryan et al., 2023), thereby potentially increasing soil microbial activity (Rodríguez et al., 2018). Changes in vegetation species dominance may also occur after fires (Purdie, 1977; Yan et al., 2020; Viana-Soto et al., 2022; Bashirzadeh et al., 2023), which could influence the amount of OM infiltrating into a cave, and the microbial composition of the overlying soils (Thoms and Gleixner, 2013; Delgado-Baquerizo et al., 2018). These factors suggest that post-fire vegetation changes are not predictable, and its impact on speleothem OM signal may be complex.

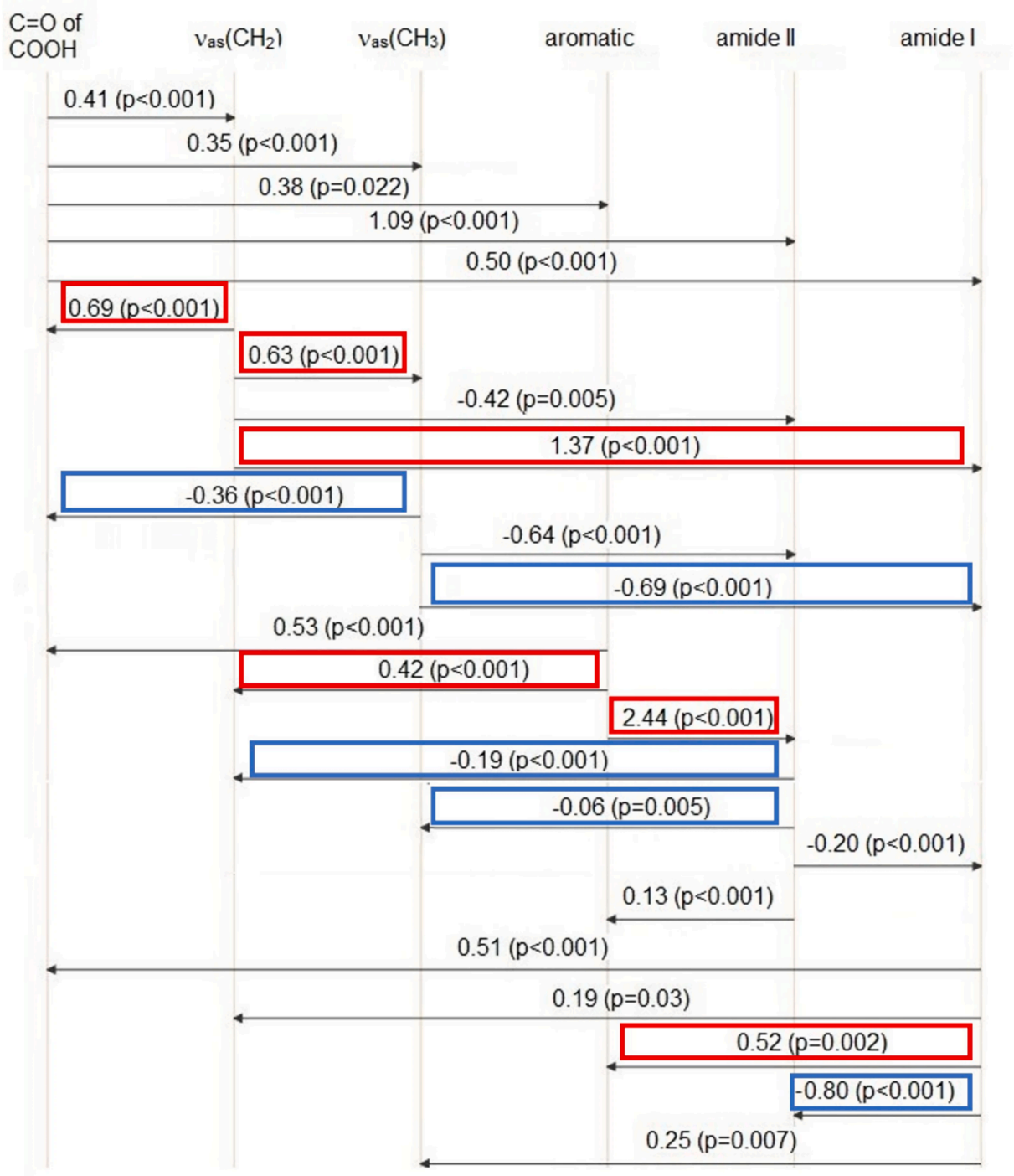

Fig. 3. Sequence diagram showing the coefficient of predictor variables to response variables (direction of relationship indicated by arrow) for significant coefficients identified through robust regression models (Table S1). For example: the uppermost arrow in the figure represents the impact of C═O of COOH on $\nu_{as}(CH_2)$ in the model that uses $\nu_{as}(CH_2)$ as the response variable. Red boxes indicate the most important predictors with positive coefficients for each variable, whilst blue boxes indicate the most important predictors with negative coefficients for each variable. Note: there are no significant negative coefficients for the model using amide I as a response variable. (For interpretation of the references to colour in this figure legend, the reader is referred to the web version of this article.)

Timeseries of OM peaks in YD-S2 obtained from IRM mapping are shown in Fig. 4, where known fire events are indicated (see Section 1.1). Trends and abrupt shifts in OM functional groups are revealed by the time series. All OM peaks appear to increase in absorbance intensity following the 1897 CE fire event (Fig. 4A). This is characterised by a rising trend in OM for approximately 15 years post-fire (~1 mm of speleothem growth). These higher OM values persist for the following ~27 years (2 mm of speleothem growth). The 1897 CE fire coincides with short-term peaks in ash-derived trace elements, as interpreted from the third principal component (McDonough et al., 2022) which is reproduced in the lower panel of Fig. 4 for comparison here. Fig. 5C reveals that the fire is also marked by higher CH_3 relative to CH_2 until approximately one-year post-fire (9200 μm DFT, Map 4). Amide II ratios also increase in the post-fire period (Fig. 5E, Map 4), while both the aromatic and amide II peaks are lowest during and after the timing of the fire event (Fig. 5D and Fig. 5E, Map 2) with no other distinct changes in

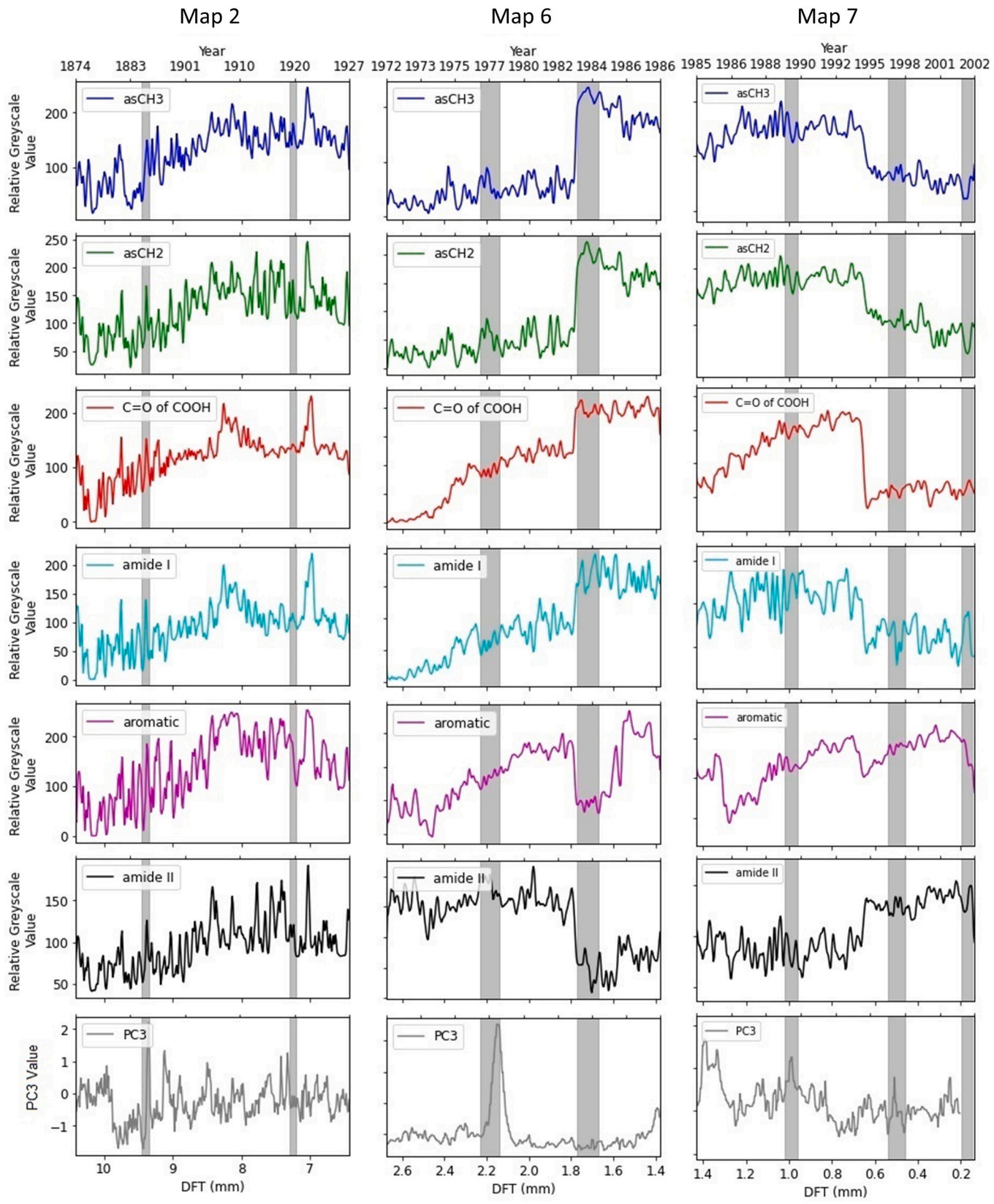

Fig. 4. Timeseries derived from maps shown in Fig. 5 for each IRM organic matter peak identified as occurring in YD-S2 in Fig. 1D. Plots represent the three larger IRM maps: A) Map 2, B) Map 6, and C) Map 7. Also shown are timeseries data of relative OM concentrations obtained from the thin section, and PC3 from McDonough et al. (2022). PC3 was related to peaks in ash-derived metals including Al, Zn, Cu and Pb as well as P in YD-S2, represent the trace element response to fire events occurring above Yonderup cave. Grey bars represent the fire events examined in this study. N.B: higher concentrations suggested by increased greyscale values in each map are relative only to the data within that map.

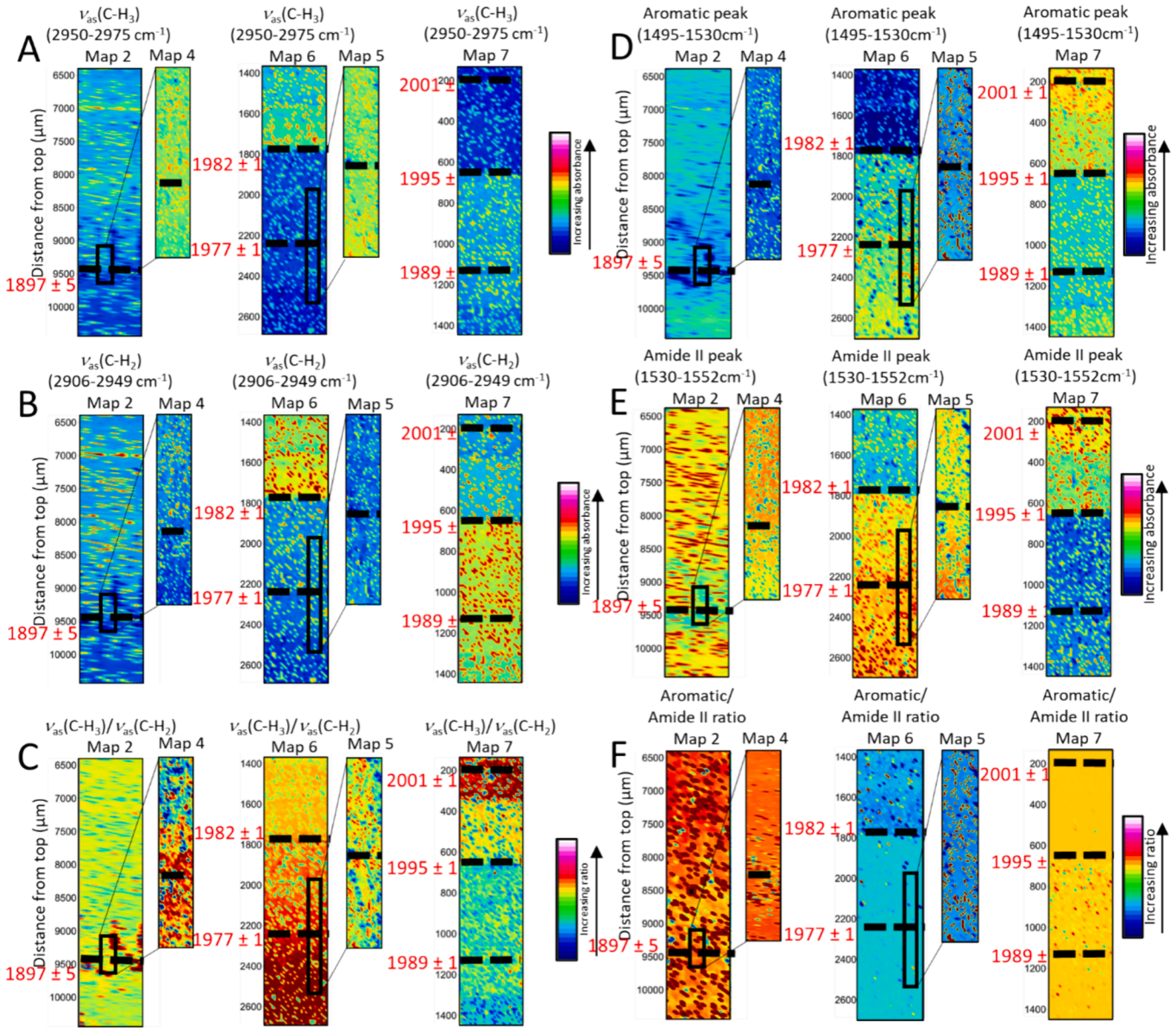

Fig. 5. Chemical maps showing the inverted second derivative peak intensity of the A) $\nu_{as}(CH_3)$ band observed at 2950–2975 cm^{-1} and the B) $\nu_{as}(CH_2)$ band observed at 2906–2949 cm^{-1} for Map 2 (low-resolution) and Map 4 (high-resolution), Map 6 (low-resolution) and Map 5 (high-resolution), and Map 7 (low-resolution). C) shows the ratio of peaks shown in A and B. D) shows the inverted second derivative peak intensity of the aromatic peak at 1495–1530 cm^{-1}, E) shows the inverted second derivative peak intensity of the amide I peak (1640–1663 cm^{-1}). E) shows the ratio of the peaks shown in D/E. High-resolution region of Map 2 and Map 6 are indicated by the black rectangle in the low-resolution maps. C) shows the ratio of the $\nu_{as}(CH_3)$/ $\nu_{as}(CH_2)$ peaks. Map 6 covers the 1977 and 1982 fire events, Map 2 covers the 1897 fire event, and Map 7 covers the 1989, 1995, and 2001 fire events. A comparison of the aromatic/amide I peaks are shown in Fig. S6. N.B: Distance from top (μm) represents distance from the youngest end of the stalagmite. Low- and high-resolution maps were performed under separate experiment and the high-resolution position shown is approximate.

the IRM OM peaks. Whilst not visible on the lower resolution Map 4, the higher resolution Map 4 shows that after approximately 1-year post-fire there is a decline in CH_3/CH_2 ratios (Fig. 5C, Map 4), and an overall post-fire increase amide II peak intensity (Fig. 5E, Map 4) which we propose to be the result of enhanced microbial activity associated with longer-chain aliphatic and nitrogen-containing OM. This suggests that trace elements may be better indicators of particularly large fire events incorporated into stalagmites compared to OM composition. The highest concentration of P incorporated into the YD-S2 record was recorded after this fire event (McDonough et al., 2022), and may be attributed to the leaching of nutrients from plant-derived ash (Chungu et al., 2020; Agbeshie et al., 2022). As phosphorus in plant ash often occurs as readily bioavailable inorganic phosphate (Condron et al., 2005), it's dissolution may have spurred post-fire microbial activity on the stalagmite, which is characterised by aliphatic OM containing a larger proportion of methylene groups (Igisu et al., 2009).

Comparing the time-series of IRM in YD-S2 in relation to fire events that occurred in 1977 CE and 1983 CE (two larger fires which burnt 500 and 800 ha respectively) against the smaller 2001 CE fire, it appears that each fire event resulted in varying changes in speleothem OM composition (Fig. 4). The 1977 CE fire resulted in a minor increase in $\nu_{as}CH_2$, $\nu_{as}CH_3$, $\nu_{as}CH_2/\nu_{as}CH_3$ ratio and amide II peaks, whilst the 1983 fire resulted in increased C═O of COOH, $\nu_{as}CH_2$, $\nu_{as}CH_3$, $\nu_{as}CH_2/\nu_{as}CH_3$ ratio and amide I peak and decreased aromatic and amide II peaks (Fig. 5B and Fig. 5C). The 1983 CE fire resulted in the largest increase in both $\nu_{as}CH_2$ and $\nu_{as}CH_3$ intensities (Fig. 4), and a clear decline in aromatic and amide II OM (Fig. 4B, Fig. 5A, Fig. 5B). A decline in the aromatic band may be the result of greater adsorption PAHs with

increased ionic strength conditions (Adeola and Forbes, 2020) which can be observed after application of biomass ash to soils (Johan et al., 2021). Whilst the shift in OM composition in 1983 CE is much clearer than that in 1977 CE, the 1977 CE fire led to a much clearer peak in trace elements, as demonstrated by PC3 from McDonough et al. (2022) (shown in Fig. 4B, lower panel). In contrast, the 2001 CE fire coincides with a decrease in absorbance band intensities for $\nu_{as}CH_2$,$\nu_{as}CH_3$, aromatic, and amide II peaks, whereas C═O of COOH and amide I peaks increased. This is consistent with observations of peaks in black and white ash which show the preservation of amide I (Fig. 2G and Fig. 2H). Post-fire shifts in OM content after the 1990 CE fire, a previously unrecorded and therefore likely small fire, inferred from changes in the inorganic chemistry of YD-S2 in McDonough et al. (2022), and after the 1996 CE fire (which represents a small fire that burnt < 30 m north of the cave), are less pronounced. This hints at their lower fire severity. Notably, however, the 1996 CE fire event displays post-fire increases in CH_3/CH_2 absorbance intensity ratios, suggesting that it caused a change in the proportion of methylene and methyl groups incorporated into the stalagmite (Fig. 5A).

The short-term impact of fire on speleothem chemistry is complex and may be controlled by factors such as meteorology, burn temperature, soil moisture, time since last fire (fuel load), and fuel type. For example, differences in fuel type and fuel quantity at the surface can cause wildfires to burn in patches and at inconsistent temperatures (Liu et al., 2021). As a result, ash and charcoal deposited into soils after fires may contain a combination of material combusted at both lower and higher temperatures, and therefore contain OM which has been exposed to varying temperatures. The 1897 CE fire event was interpreted to be a high intensity fire (McDonough et al., 2022), however, it is characterised in the stalagmite by a large increase in P, which has shown to be found in higher concentrations in leachates of less-well-combusted ashes from Yanchep National Park (Campbell et al., 2023). This suggests deposition of large amounts of incompletely combusted biomass above the cave. This may have been blown onto the site from areas that burned at lower temperature, or heterogeneity in the fire severity may have resulted in a mosaic of more- and less-completely combusted biomass. In contrast, the minimal impact of the 1996 CE fire on the OM concentration of YD-S2 reflects the small burn zone on the boundary of the cave area, as recorded by the Department of Biodiversity (2020). These observations support those of McDonough et al. (2022) who concluded that inconsistencies in the inorganic composition of YD-S2 after fire events were likely to result from differences in burn severity, as well as climate conditions during and after the fire event.

3.3.2. *Nanoporosity and OM location within YD-S2*

The HRTEM observations revealed that calcite crystals are characterized by alignment of nanopores that seem to follow crystallographic directions. Their morphology appears to be that of the cleavage rhombohedron (the Miller-Bravais {1 0 $\bar{1}$ 4} form; Fig. 6A and B), which is characterized by marked F-(flat) faces (Aquilano et al., 2013). The nanopores are aligned in a direction normal to the {1 0 $\bar{1}$ 4} faces, which is most likely the crystal growth direction (Fig. 6A). The {1 0 $\bar{1}$ 4} is the cleavage rhombohedron, which is the "reference form" of calcite morphology. The characteristic shape of the nanopores and their alignment along the crystal growth suggest that organic molecules may be accommodated in nanopores that exist on the {1 0 $\bar{1}$ 4} faces. Although the EDS analyses do not highlight organic molecules as FTIR does, the phosphorous EDS map of the area highlighted by the HAADF image (Fig. 6C, D) suggest that phosphate is accommodated within the

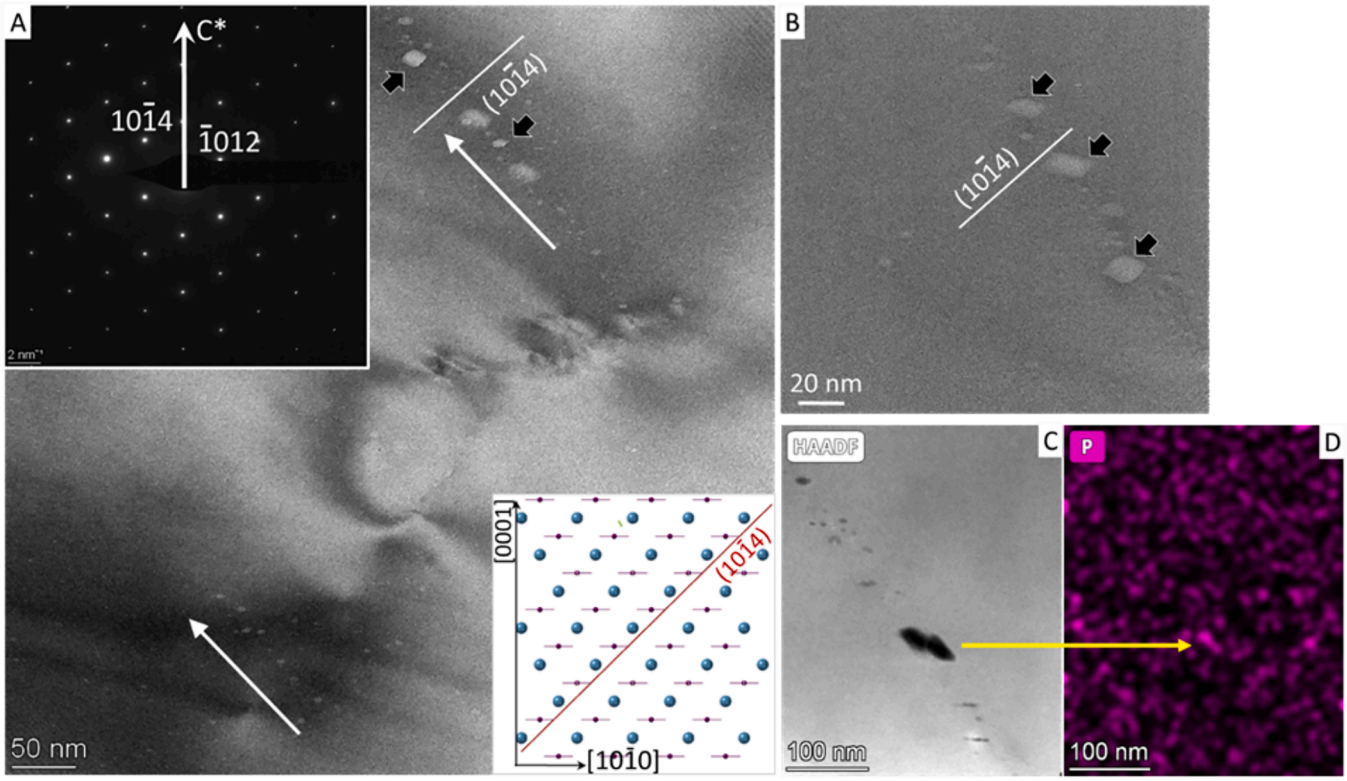

Fig. 6. A) [1 0 $\bar{1}$ 0] HRTEM images of an electron transparent lamella cut towards the top of the "1897 fire layer" illustrated in McDonough et al. (2022), with the selected area diffraction pattern and insert showing the calcite lattice corresponding to this projection. 1 0 $\bar{1}$ 4 and $\bar{1}$ 0 1 2 corresponding to the cleavage {1 0 $\bar{1}$ 4} and steep rhombohedron {$\bar{1}$ 0 1 2} respectively, are indicated. The most notable feature is the presence of nano-pores with a morphology related to the {10 $\bar{1}$ 4} form, as indicated by the black arrows (B) and their alignment in a direction perpendicular to {1 0 $\bar{1}$ 4}, as indicated by the white arrows. The {1 0 $\bar{1}$ 4} is a F-form (flat faces) that dominates the morphology of calcite crystals in nature. C) is the HAADF of the area in B. and D) is the P map obtained by EDS which shows that P is related to the nanoporosity.

pervasive nanoporosity of the specimen. Despite the low statistics of the P counts measured by EDS, P was previously detected by Laser Ablation Inductively Coupled Plasma Mass spectrometry and Synchrotron X-Ray Fluorescence in association with the 1897 fire layer (McDonough et al., 2022). Campbell et al. (2023) attributed P in YD-S2 as derived from combusted biomass. Thus, it is reasonable to infer that most of the OM detected by Synchrotron IRM is hosted in rhombohedra-shaped nanopores, which are clearly a primary feature, due to their morphology dictated by crystallographic directions and small sizes.

Sets of nanopores are spaced hundreds of nanometres apart (Fig. 6A), which contrasts with an estimated annual growth rate of the stalagmite of 76.7 μm ± 30.3 (1σ). The OM accommodated in the nanopores of YD-S2, therefore, may not mark annual changes, at least near the fire layer. This contrasts with observations in stalagmites retrieved elsewhere, where OM in some samples can define annual banding (Baker et al., 2021). The HRTEM observations of YD-S2 suggest that Synchrotron IRM, which has a resolution in of the order of approximately 5 μm or more, most likely averaged OM signals detected over (potentially hundreds of) nanopores aligned perpendicular to {1 0 $\bar{1}$ 4} faces. Nevertheless, the Synchrotron IRM mapping is still a most promising technique, as it seems to show some preferred orientation in the ratio of the second derivative peak intensity for the $\nu_{as}(CH_3)$ and the $\nu_{as}(CH_2)$ bands (Fig. 5). By comparing Fig. 5 and Fig. 6A, knowing that both the thick section and the lamella are oriented along the stalagmite growth axis, the IRM maps appear to highlight a preferential distribution of organic molecules for the 1897 CE fire roughly perpendicular to {1 0 $\bar{1}$ 4} faces, which is clear in Map 4 of Fig. 5. The IRM maps (Fig. 5) may therefore show a pattern of OM incorporation in nanopores that form whilst calcite crystals are growing independently of seasonality. By contrast, the annual layering of YD-S2 defined by trace elements (McDonough et al., 2022), suggests that trace elements may be incorporated at lattice sites or defect sites, rather than in the nanopores.

Interestingly, by coupling Confocal Laser Scanning Microscopy and FTIR with a focal plane array detector, Kost et al. (2023) found that in three actively growing stalagmites, growth layers with high(er) concentrations of organic matter did not feature a higher density of defects or fluid inclusions at a resolution of the order of hundreds of micrometres. The nanoscale data presented in our study reveals that the OM may be absorbing to the surface of the growing crystal, initially occluded from the (nano)crystal(s) and eventually becoming incorporated within nanopores.

4. Conclusion

This study demonstrates the successful use of Synchrotron IRM in mapping stalagmite OM composition over very short (<1 year) to longer time periods (decades) at very high resolution (5–50 μm). We used known fire events as case studies of discrete periods of environmental changes. Our study utilised FTIR analysis of reference materials, including precipitated $CaCO_3$, vegetation, soil, and ash samples for the robust identification of specific absorbance bands associated with CO_3^{2-} and OM peaks. This approach serves as a framework for interpreting the organic matter signal in stalagmite YD-S2 and, potentially, for other stalagmites or environmental data.

Our analysis revealed that the OM in YD-S2 originates from different sources, potentially including partially burnt biomass from ash, soil, microbial biomass and terrestrial plant material. We identify a lower proportion of aromatic OM groups in YD-S2, notably an almost complete absence of the aromatic peak at 1610 cm^{-1}, compared to vegetation and IHSS standards. YD-S2 displays a dominant signal from amide (protein) OM groups, suggesting a dominant microbial signal, with robust regression modelling highlighting the association of these amide groups (amide I and amide II) to aliphatic CH_2 and aromatic groups respectively. These different associations indicate variability in the sources and processing of compounds associated with these groups. Our data suggests that this OM is incorporated in nanopores that form whilst calcite crystals are growing, at the spatial scale of hundreds of nanometers.

The findings suggest that in some cases, OM may not serve as the most robust or reliable proxy for fire events, given the supply issue observed in Fig. 2 where burning results in the loss of OM. This may be related to the intensity of the fire, where a larger fire burning at high intensity may result in the removal of OM, in which case trace elements leached from ash may be a better indicator of fire events. For example, the observed lack of an abrupt shift in OM composition (in the IRM data) after the inferred 1897 CE fire suggests likely complete combustion and removal of OM from overlying ash and soil, with no observed OM signal transported into the stalagmite. In contrast, a clear inorganic signal of this event is observed in the trace element analysis by McDonough et al. (2022). A decline in CH_3/CH_2 ratios approximately 1-year post-fire, linked to the incorporation of high amounts of ash-derived P, indicate enhanced microbial activity on the stalagmite surface. TEM analysis supports that this OM may be hosted in nanopores, however, this requires further research. Furthermore, fluctuations in CH_3/CH_2 ratios after the 1977 CE, 1983 CE and 2001 CE fires indicate variability in the microbial activity response post-fire. variability in the response of OM functional groups to fires underscores the complexity of the system. Further speleothem OM research encompassing diverse regions, caves, climate and vegetation types, with accompanying ‘ground truthing’ of the microbial response use, for example eDNA, would aid in unravelling the multifaceted factors contributing to the observed variability in results and aid in refining the utilisation of OM as an environmental proxy in speleothems.

Our use of reference materials and Synchrotron IRM distinguish our work from the emerging body of FTIR analysis of speleothems. The use of reference materials allowed us to identify key compounds, and how they change between vegetation, soil, ash, and the speleothem. This was found to be more reliable than using published peak locations, as peaks were shown to shift in wavenumbers (Fig. 1B), resulting in a more robust interpretation of the results. The identification of FTIR peaks relevant to speleothem OM will assist future researchers looking to analyse speleothem OM composition using Synchrotron IRM or FTIR techniques. The use of Synchrotron radiation allowed for better detection of the low concentration OM in YD-S2, allowing for identification of compounds which may have been undetectable in YD-S2 using globar FTIR. Our use of the micro-ATR methodology allowed for the mapping of OM in YD-S2 at a resolution unmatched in the literature. Combined, this represents a significant step forward in the non-destructive analysis of OM in speleothems.

Funding

This work was funded through the Australian Research Council Discovery Project DP200100203. The authors acknowledge the support of ANSTO in providing access to instruments, capabilities and facilities used in this study via portal access proposals 17905 and 18777. The use of the TEM facility was supported by the grants no. VEKOP-2.3.3-15-2016-00002 and VEKOP-2.3.2-16-2016-00011 of the European Structural and Investment Funds.

CRediT authorship contribution statement

Liza K. McDonough: Writing – review & editing, Writing – original draft, Visualization, Methodology, Investigation, Formal analysis, Data curation. **Micheline Campbell:** Writing – review & editing, Resources, Project administration, Methodology, Investigation. **Pauline C. Treble:** Writing – review & editing, Supervision, Project administration, Funding acquisition, Conceptualization. **Christopher Marjo:** Writing – review & editing, Methodology, Investigation. **Silvia Frisia:** Writing – review & editing, Methodology, Investigation, Data curation, Conceptualization. **Jitraporn Vongsvivut:** Writing – review & editing,

Methodology, Data curation. **Annaleise R. Klein:** Writing – review & editing, Methodology, Data curation. **Viktoria Kovacs-Kis:** Writing – review & editing, Data curation. **Andy Baker:** Writing – review & editing, Supervision, Resources, Project administration, Investigation, Data curation, Conceptualization.

Declaration of competing interest

The authors declare that they have no known competing financial interests or personal relationships that could have appeared to influence the work reported in this paper.

Data availability

A spectral database of FTIR reference materials including soils from Macleay, Calgardup, Yanchep and Golgotha, YD-S2 speleothem, vegetation reference materials and bushfire ash are provided at DOI https://doi.org/10.6084/m9.figshare.25323205.

Acknowledgements

The authors thank Peter Reece for helpful discussions on the differences in calcite crystal vs powder FTIR spectra. We also thank Mark Tobin for his assistance with Synchrotron IRM analyses. Thanks to Katie Coleborn and Anne Wood for the collection and preparation of vegetation samples from SW WA, Pauline Grierson for collection of ash samples, Calgardup Caves and Yanchep Caves for their assistance and to Henri Wong for supplying precipitated $CaCO_3$ powder. SF is grateful to György Zoltán Radnóczi (CER) for obtaining the highest possible quality TEM lamellae and Béla Pécz for both granting access at the FIB and HREM and technical advice.

Appendix A. Supplementary data

Supplementary data to this article can be found online at https://doi.org/10.1016/j.orggeochem.2024.104842.

References

Adeola, A.O., Forbes, P.B.C., 2020. Optimization of the sorption of selected polycyclic aromatic hydrocarbons by regenerable graphene wool. Water Science and Technology 80, 1931–1943.
Agbeshie, A.A., Abugre, S., Atta-Darkwa, T., Awuah, R., 2022. A review of the effects of forest fire on soil properties. Journal of Forestry Research 33, 1419–1441.
Anderson, C.R., Peterson, M.E., Frampton, R.A., Bulman, S.R., Keenan, S., Curtin, D., 2018. Rapid increases in soil pH solubilise organic matter, dramatically increase denitrification potential and strongly stimulate microorganisms from the Firmicutes phylum. PeerJ 6, e6090.
Aquilano, D., Benages-Vilau, R., Bruno, M., Rubbo, M., Massaro, F.R., 2013. Positive hk.l and negative hk.l̄ forms of calcite (CaCO3) crystal. New open questions from the evaluation of their surface energies. CrystEngComm 15, 4465–4472.
Argiriadis, E., Denniston, R.F., Barbante, C., 2019. Improved polycyclic aromatic hydrocarbon and n-alkane determination in speleothems through cleanroom sample processing. Analytical Chemistry 91, 7007–7011.
Argiriadis, E., Denniston, R.F., Ondei, S., Bowman, D.M.J.S., Genuzio, G., Nguyen, H.Q. A., Thompson, J., Baltieri, M., Azenon, J., Cugley, J., Woods, D., Humphreys, W.F., Barbante, C., 2024. Polycyclic aromatic hydrocarbons in tropical Australian stalagmites: a framework for reconstructing paleofire activity. Geochimica et Cosmochimica Acta 366, 250–266.
Arocena, J.M., Pawluk, S., Dudas, M.J., Gajdostik, A., 1995. In situ investigation of soil organic matter aggregates using infrared microscopy. Canadian Journal of Soil Science 75, 327–332.
Arrizabalaga, I., Gómez-Laserna, O., Carrero, J.A., Bustamante, J., Rodríguez, A., Arana, G., Madariaga, J.M., 2015. Diffuse reflectance FTIR database for the interpretation of the spectra obtained with a handheld device on built heritage materials. Analytical Methods 7, 1061–1070.
Baker, A., Mariethoz, G., Comas-Bru, L., Hartmann, A., Frisia, S., Borsato, A., Treble, P. C., Asrat, A., 2021. The Properties of annually laminated stalagmites-A global synthesis. Reviews of Geophysics 59, e2020RG000722.
Baldini, J.U.L., McDermott, F., Baker, A., Baldini, L.M., Mattey, D.P., Railsback, L.B., 2005. Biomass effects on stalagmite growth and isotope ratios: a 20th century analogue from Wiltshire, England. Earth and Planetary Science Letters 240, 486–494.
Bashirzadeh, M., Abedi, M., Shefferson, R.P., Farzam, M., 2023. Post-Fire Recovery of Plant Biodiversity Changes Depending on Time Intervals since Last Fire in Semiarid Shrublands. Fire 6, 103.
Benning, L.G., Phoenix, V.R., Yee, N., Konhauser, K.O., 2004. The dynamics of cyanobacterial silicification: an infrared micro-spectroscopic investigation. Geochimica et Cosmochimica Acta 68, 743–757.
Blyth, A.J., Baker, A., Collins, M.J., Penkman, K.E.H., Gilmour, M.A., Moss, J.S., Genty, D., Drysdale, R.N., 2008. Molecular organic matter in speleothems and its potential as an environmental proxy. Quaternary Science Reviews 27, 905–921.
Blyth, A.J., Hartland, A., Baker, A., 2016. Organic proxies in speleothems – New developments, advantages and limitations. Quaternary Science Reviews 149, 1–17.
Campbell, M., McDonough, L., Treble, P., Baker, A., Kosarac, N., Coleborn, K., Wynn, P. M., Schmitt, A.K., 2023. A review of speleothems as archives for palaeofire proxies, with Australian case studies. Reviews of Geophysics 61, e2022RG000790.
Cheng, H., Edwards, R.L., Sinha, A., Spötl, C., Yi, L., Chen, S., Kelly, M., Kathayat, G., Wang, X., Li, X., Kong, X., Wang, Y., Ning, Y., Zhang, H., 2016. The Asian monsoon over the past 640,000 years and ice age terminations. Nature 534, 640–646.
Chirenje, T., Rivero, C., Ma, L.Q., 2002. Leachability of Cu and Ni in wood ash-amended soil as impacted by humic and fulvic acid. Geoderma 108, 31–47.
Chungu, D., Ng'andwe, P., Mubanga, H., Chileshe, F., 2020. Fire alters the availability of soil nutrients and accelerates growth of Eucalyptus grandis in Zambia. Journal of Forestry Research 31, 1637–1645.
Coleborn, K., Spate, A., Tozer, M., Andersen, M.S., Fairchild, I.J., MacKenzie, B., Treble, P.C., Meehan, S., Baker, A., Baker, A., 2016. Effects of wildfire on long-term soil CO2 concentration: implications for karst processes. Environmental Earth Sciences 75, 330.
Coleborn, K., Baker, A., Treble, P.C., Andersen, M.S., Baker, A., Tadros, C.V., Tozer, M., Fairchild, I.J., Spate, A., Meehan, S., 2018. The impact of fire on the geochemistry of speleothem-forming drip water in a sub-alpine cave. Science of the Total Environment 642, 408–420.
Condron, L.M., Turner, B.L., Cade-Menun, B.J., 2005. Chemistry and Dynamics of Soil Organic Phosphorus. In: Sims, T.J., Sharpley, A.N. (Eds.), Phosphorus: Agriculture and the Environment. American Society of Agronomy, Crop Science Society of America and Soil Science Society of America, Wisconsin, pp. 87–121.
Delgado-Baquerizo, M., Reith, F., Dennis, P.G., Hamonts, K., Powell, J.R., Young, A., Singh, B.K., Bissett, A., 2018. Ecological drivers of soil microbial diversity and soil biological networks in the Southern Hemisphere. Ecology 99, 583–596.
[dataset] Department of Biodiversity, Conservation and Attractions, 2020. DBCA Fire History (DBCA-060). Data WA. Retrieved from https://catalogue.data.wa.gov.au/dataset/dbca-fire-history.
Department of Environment and Conservation, 2010. Parks and Reserves of Yanchep and Neerabup Draft Management Plan 2010. Retrieved from https://library.dbca.wa.gov.au/static/FullTextFiles/025376.pdf.
Elias, V.O., Simoneit, B.R.T., Cordeiro, R.C., Turcq, B., 2001. Evaluating levoglucosan as an indicator of biomass burning in Carajás, amazônia: a comparison to the charcoal record. Geochimica et Cosmochimica Acta 65, 267–272.
Fisher, T., Hajaligol, M., Waymack, B., Kellogg, D., 2002. Pyrolysis behavior and kinetics of biomass derived materials. Journal of Analytical and Applied Pyrolysis 62, 331–349.
Frisia, S., Borsato, A., 2010. Chapter 6 karst. In: Alonso-Zarza, A.M., Tanner, L.H. (Eds.), Developments in Sedimentology 61. Elsevier, Oxford, pp. 269–318.
Frisia, S., Borsato, A., Hartland, A., Faraji, M., Demeny, A., Drysdale, R.N., Marjo, C.E., 2022. Crystallization pathways, fabrics and the capture of climate proxies in speleothems: Examples from the tropics. Quaternary Science Reviews 297, 107833.
Galván-Ruiz, M., Hernández, J., Baños, L., Noriega-Montes, J., Rodríguez-García, M.E., 2009. Characterization of calcium carbonate, calcium oxide, and calcium hydroxide as starting point to the improvement of lime for their use in construction. Journal of Materials in Civil Engineering 21, 694–698.
Gao, C., Cong, J., Sun, Y., Han, D., Wang, G., 2022. Variability in pyrogenic carbon properties generated by different burning temperatures and peatland plant litters: implication for identifying fire intensity and fuel types. International Journal of Wildland Fire 31, 395–408.
González-Pérez, J.A., González-Vila, F.J., Almendros, G., Knicker, H., 2004. The effect of fire on soil organic matter—a review. Environment International 30, 855–870.
Hartland, A., Fairchild, I.J., Lead, J.R., Dominguez-Villar, D., Baker, A., Gunn, J., Baalousha, M., Ju-Nam, Y., 2010. The dripwaters and speleothems of Poole's Cavern: a review of recent and ongoing research. Cave and Karst Science 36, 37–46.
Hartland, A., Fairchild, I.J., Lead, J.R., Borsato, A., Baker, A., Frisia, S., Baalousha, M., 2012. From soil to cave: Transport of trace metals by natural organic matter in karst dripwaters. Chemical Geology 304–305, 68–82.
He, Z., Mao, J., Honeycutt, C.W., Ohno, T., Hunt, J.F., Cade-Menun, B.J., 2009. Characterization of plant-derived water extractable organic matter by multiple spectroscopic techniques. Biology and Fertility of Soils 45, 609–616.
Homann, J., Oster, J.L., de Wet, C.B., Breitenbach, S.F.M., Hoffmann, T., 2022. Linked fire activity and climate whiplash in California during the early Holocene. Nature Communications 13, 7175.
Igisu, M., Ueno, Y., Shimojima, M., Nakashima, S., Awramik, S.M., Ohta, H., Maruyama, S., 2009. Micro-FTIR spectroscopic signatures of bacterial lipids in Proterozoic microfossils. Precambrian Research 173, 19–26.
Igisu, M., Ueno, Y., Takai, K., 2018a. FTIR microspectroscopy of carbonaceous matter in ~ 3.5 Ga seafloor hydrothermal deposits in the North Pole area, Western Australia. Progress in Earth and Planetary Science 5, 85.
Igisu, M., Yokoyama, T., Ueno, Y., Nakashima, S., Shimojima, M., Ohta, H., Maruyama, S., 2018b. Changes of aliphatic C-H bonds in cyanobacteria during experimental thermal maturation in the presence or absence of silica as evaluated by FTIR microspectroscopy. Geobiology 16, 412–428.

Jardine, P.E., Abernethy, F.A.J., Lomax, B.H., Gosling, W.D., Fraser, W.T., 2017. Shedding light on sporopollenin chemistry, with reference to UV reconstructions. Review of Palaeobotany and Palynology 238, 1–6.
Johan, P.D., Ahmed, O.H., Omar, L., Hasbullah, N.A., 2021. Charcoal and sago bark ash on pH buffering capacity and phosphorus leaching. Agronomy 11, 2223.
Kamnev, A.A., Dyatlova, Y.A., Kenzhegulov, O.A., Fedonenko, Y.P., Evstigneeva, S.S., Tugarova, A.V., 2023. Fourier Transform Infrared (FTIR) Spectroscopic Study of Biofilms Formed by the Rhizobacterium Azospirillum baldaniorum Sp245: Aspects of Methodology and Matrix Composition. Molecules 28, 1949.
Kang, J.-H., Hwang, H., Lee, S.-J., Choi, S.-D., Kim, J.-S., Hong, S., Hur, S.D., Baek, J.-H., 2021. Record of North American boreal forest fires in northwest Greenland snow. Chemosphere 276, 130187.
Kleber, M., 2022. Soil organic matter: Composition. In: Goss, M.J., Oliver, M. (Eds.), Encyclopedia of Soils in the Environment, second ed. Elsevier, Oxford, pp. 58–67.
Kost, O., Sliwinski, J., Gies, N., Lueder, M., Stoll, H., 2023. The influence of fluid inclusions, organics, and calcite fabric on trace element distributions in stalagmites. Frontiers in Earth Science 11, 1–21.
Kozlowski, T.T., 2002. Physiological ecology of natural regeneration of harvested and disturbed forest stands: implications for forest management. Forest Ecology and Management 158, 195–221.
Lamichhane, S., Bal Krishna, K.C., Sarukkalige, R., 2016. Polycyclic aromatic hydrocarbons (PAHs) removal by sorption: a review. Chemosphere 148, 336–353.
Li, X., Hu, C., Huang, J., Xie, S., Baker, A., 2014. A 9000-year carbon isotopic record of acid-soluble organic matter in a stalagmite from Heshang Cave, central China: paleoclimate implications. Chemical Geology 388, 71–77.
Lin, R., Patrick Ritz, G., 1993. Studying individual macerals using i.r. microspectrometry, and implications on oil versus gas/condensate proneness and "low-rank" generation. Organic Geochemistry 20, 695–706.
Liu, N., Lei, J., Gao, W., Chen, H., Xie, X., 2021. Combustion dynamics of large-scale wildfires. Proceedings of the Combustion Institute 38, 157–198.
Madsen, D., Azeem, H.A., Sandahl, M., van Hees, P., Husted, B., 2018. Levoglucosan as a tracer for smouldering fire. Fire Technology 54, 1871–1885.
Mangold, H.K., 1969. Aliphatic Lipids. In: Stahl, E. (Ed.), Thin-Layer Chromatography: A Laboratory Handbook. Springer, Berlin Heidelberg, Berlin, Heidelberg, pp. 363–421.
Martínez-Pillado, V., Yusta, I., Iriarte, E., Álvaro, A., Ortega, N., Aranburu, A., Arsuaga, J. L., 2020. The red coloration of Goikoetxe Cave's speleothems (Busturia, Spain): An indicator of paleoclimatic changes. Quaternary International 566–567, 141–151.
Masto, R.E., Sarkar, E., George, J., Jyoti, K., Dutta, P., Ram, L.C., 2015. PAHs and potentially toxic elements in the fly ash and bed ash of biomass fired power plants. Fuel Processing Technology 132, 139–152.
Mastrolonardo, G., Francioso, O., Di Foggia, M., Bonora, S., Rumpel, C., Certini, G., 2014. Application of thermal and spectroscopic techniques to assess fire-induced changes to soil organic matter in a Mediterranean forest. Journal of Geochemical Exploration 143, 174–182.
Mastrolonardo, G., Rumpel, C., Forte, C., Doerr, S.H., Certini, G., 2015. Abundance and composition of free and aggregate-occluded carbohydrates and lignin in two forest soils as affected by wildfires of different severity. Geoderma 245–246, 40–51.
McDonough, L.K., Treble, P.C., Baker, A., Borsato, A., Frisia, S., Nagra, G., Coleborn, K., Gagan, M.K., Zhao, J.-X., Paterson, D., 2022. Past fires and post-fire impacts reconstructed from a southwest Australian stalagmite. Geochimica et Cosmochimica Acta 325, 258–277.
Montecchio, D., Francioso, O., Carletti, P., Pizzeghello, D., Chersich, S., Previtali, F., Nardi, S., 2006. Thermal analysis (TG-DTA) and drift spectroscopy applied to investigate theevolution of humic acids in forest soil at different vegetation stages. Journal of Thermal Analysis and Calorimetry 83, 393–399.
Moropoulou, A., Bakolas, A., Aggelakopoulou, E., 2001. The effects of limestone characteristics and calcination temperature to the reactivity of the quicklime. Cement and Concrete Research 31, 633–639.
Moya, D., González-De Vega, S., Lozano, E., García-Orenes, F., Mataix-Solera, J., Lucas-Borja, M.E., de las Heras, J., 2019. The burn severity and plant recovery relationship affect the biological and chemical soil properties of Pinus halepensis Mill. stands in the short and mid-terms after wildfire. Journal of Environmental Management 235, 250–256.
Nagra, G., Treble, P.C., Andersen, M.S., Fairchild, I.J., Coleborn, K., Baker, A., 2016. A post-wildfire response in cave dripwater chemistry. Hydrology and Earth System Sciences 20, 2745–2758.
Nagra, G., Treble, P.C., Andersen, M.S., Bajo, P., Hellstrom, J., Baker, A., 2017. Dating stalagmites in mediterranean climates using annual trace element cycles. Scientific Reports 7, 621.
Naumann, D., Fijala, V., Labischinski, H., 1988. The differentiation and identification of pathogenic bacteria using FT-IR and multivariate statistical analysis. Microchimica Acta 94, 373–377.
Nikolenko, N.V., 2001. The surface properties of calcite: an adsorption model with orbital control. Adsorption Science & Technology 19, 237–244.
Nuzzo, A., Buurman, P., Cozzolino, V., Spaccini, R., Piccolo, A., 2020. Infrared spectra of soil organic matter under a primary vegetation sequence. Chemical and Biological Technologies in Agriculture 7, 1–12.
O'Donnell, A.J., McCaw, W.L., Cook, E.R., Grierson, P.F., 2021. Megadroughts and pluvials in southwest Australia: 1350–2017 CE. Climate Dynamics 57, 1817–1831.
Olk, D.C., Brunetti, G., Senesi, N., 2000. Decrease in humification of organic matter with intensified lowland rice cropping a wet chemical and spectroscopic investigation. Soil Science Society of America Journal 64, 1337–1347.
Pearson, A.R., Hartland, A., Frisia, S., Fox, B.R.S., 2020. Formation of calcite in the presence of dissolved organic matter: Partitioning, fabrics and fluorescence. Chemical Geology 539, 119492.
Pejcic, B., Shelton, T., leGras, M., Laukamp, C., Francis, N., Lau, I., 2021. Mid infrared spectral library. CSIRO report EP2021-1148.
Perrette, Y., Poulenard, J., Saber, A.-I., Fanget, B., Guittonneau, S., Ghaleb, B., Garaudee, S., 2008. Polycyclic aromatic hydrocarbons in stalagmites: occurrence and use for analyzing past environments. Chemical Geology 251, 67–76.
Playford, P., Cockbain, A., Low, G., 1976. Geology of the Perth Basin Western Australia. Geological Survey of Western Australia Bulletin 124.
Purdie, R., 1977. Early stages of regeneration after burning in dry sclerophyll vegetation. II. Regeneration by seed germination. Australian Journal of Botany 25, 35–46.
Rodríguez, J., González-Pérez, J.A., Turmero, A., Hernández, M., Ball, A.S., González-Vila, F.J., Arias, M.E., 2018. Physico-chemical and microbial perturbations of Andalusian pine forest soils following a wildfire. Science of the Total Environment 634, 650–660.
Ryan, R., Dosseto, A., Lemarchand, D., Dlapa, P., Thomas, Z., Simkovic, I., Bradstock, R., 2023. Boron isotopes and FTIR spectroscopy to identify past high severity fires. Catena 222, 106887.
Savitzky, A., Golay, M.J.E., 1964. Smoothing and Differentiation of Data by Simplified Least Squares Procedures. Analytical Chemistry 36, 1627–1639.
Schneider, C.A., Rasband, W.S., Eliceiri, K.W., 2012. NIH Image to ImageJ: 25 years of image analysis. Nature Methods 9, 671–675.
Seabold, S., Perktold, J., 2010. Statsmodels: Econometric and Statistical Modelling with Python. In: Proceedings of the 9th Python in Science Conference, vol. 57, pp. 92-96.
Shtober-Zisu, N., Wittenberg, L., 2021. Wildfires as a weathering agent of carbonate rocks. Minerals 11, 1091.
Simoneit, B.R.T., Schauer, J.J., Nolte, C.G., Oros, D.R., Elias, V.O., Fraser, M.P., Rogge, W.F., Cass, G.R., 1999. Levoglucosan, a tracer for cellulose in biomass burning and atmospheric particles. Atmospheric Environment 33, 173–182.
Solomon, D., Lehmann, J., Kinyangi, J., Liang, B., Schäfer, T., 2005. Carbon K-Edge NEXAFS and FTIR-ATR spectroscopic investigation of organic carbon speciation in soils. Soil Science Society of America Journal 69, 107–119.
Soong, J.L., Parton, W.J., Calderon, F., Campbell, E.E., Cotrufo, M.F., 2015. A new conceptual model on the fate and controls of fresh and pyrolized plant litter decomposition. Biogeochemistry 124, 27–44.
Stanienda-Pilecki, K., 2019. The importance of Fourier transform infrared spectroscopy in the identification of carbonate phases differentiated in magnesium content. Spectroscopy-US 34, 32–42.
Stevenson, F.J., 1994. Humus chemistry: genesis, composition, reactions. John Wiley, New York.
Thoms, C., Gleixner, G., 2013. Seasonal differences in tree species' influence on soil microbial communities. Soil Biology and Biochemistry 66, 239–248.
Viana-Soto, A., Okujeni, A., Pflugmacher, D., García, M., Aguado, I., Hostert, P., 2022. Quantifying post-fire shifts in woody-vegetation cover composition in Mediterranean pine forests using Landsat time series and regression-based unmixing. Remote Sensing of Environment 281, 113239.
Wakeham, S.G., Schaffner, C., Giger, W., 1980. Polycyclic aromatic hydrocarbons in Recent lake sediments—I. Compounds having anthropogenic origins. Geochimica et Cosmochimica Acta 44, 403–413.
Wynn, P.M., Brocks, J.J., 2014. A framework for the extraction and interpretation of organic molecules in speleothem carbonate. Rapid Communications in Mass Spectrometry 28, 845–854.
Yan, Y., Dai, Q., Hu, G., Jiao, Q., Mei, L., Fu, W., 2020. Effects of vegetation type on the microbial characteristics of the fissure soil-plant systems in karst rocky desertification regions of SW China. Science of the Total Environment 712, 136543.
Yang, H., Ding, W., Zhang, C.L., Wu, X., Ma, X., He, G., Huang, J., Xie, S., 2011. Occurrence of tetraether lipids in stalagmites: Implications for sources and GDGT-based proxies. Organic Geochemistry 42, 108–115.